Supplementary Information (SI) for Materials Horizons.

Supplementary material of

Differentiating the origin of local charge transfer in oxides and hybrid halides by accumulating charge

Chenxi Wang[a,f], Panithan Sriboriboon[a,b], Owoong Kwon[a], Seo-Ryeong Lee[c], Myeong Seop Song[d], Jin-Wook Lee[c,e], Seung Chul Chae[d], Yunseok Kim[a,b,*]

[a] School of Advanced Materials Science and Engineering, Sungkyunkwan University (SKKU), Suwon 16419, Republic of Korea

[b] Research Center for Advanced Materials Technology, Core Research Institute, Suwon 16419, Republic of Korea

[c] Department of Nano Science and Technology and Department of Nanoengineering, SKKU Advanced Institute of Nanotechnology (SAINT), Sungkyunkwan University, Suwon 16419, Republic of Korea

[d] Department of Physics Education, Seoul National University, Seoul 08826, Republic of Korea

[e] SKKU Institute of Energy Science & Technology (SIEST), Sungkyunkwan University, Suwon 16419, Republic of Korea

[f] College of Physics and Information Engineering, Fuzhou University, Fuzhou 350116, No. 2 Wulongjiang Avenue, Minhou County, Fuzhou City, Fujian Province, China

---

[*] Corresponding author.
E-mail addresses: yunseokkim@skku.edu (Y. Kim)

Supplementary Note 1 . Phase-field model for ferroelectric thin films.

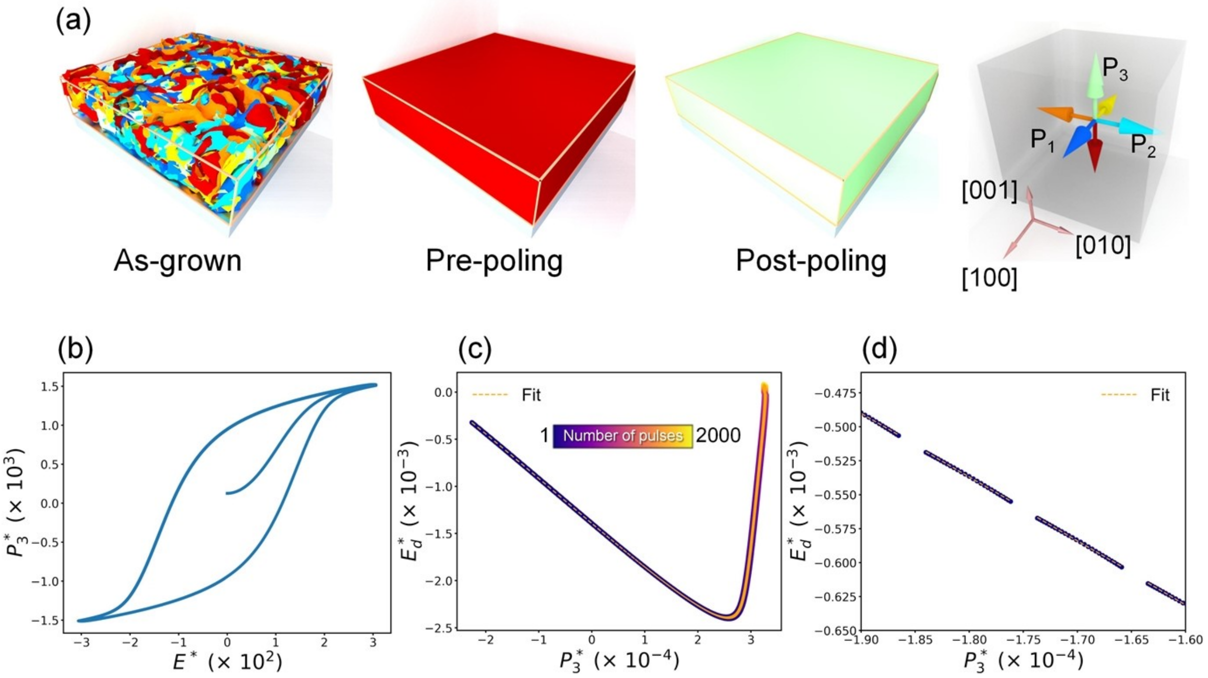

Fig. S1. Phase-field simulation results. (a**)**. Domain structure of the (left) as-grown, (middle) pre-poled and (right) post-poled PZT thin films. (b). Calculated P-E hysteresis loops subjected to AFM tip-induced electric field. (c). Relations between the internal field and polarization. (d). Zoomed in figure of (c).

Phase-field model for ferroelectric thin films in this work considers the total free energy as:

$$F = \oiiint (f_L + f_{elas} + f_{dip} + f_{dep} + f_{grad})dV \quad , \qquad \text{(S1)}$$

where f_L, f_{elas}, f_{dip}, f_{dep}, f_{grad} are the bulk Landau, elastic, multiple dipole-dipole interaction, average depolarization and gradient free energy densities, respectively. They are expressed using Einstein notion, in which repeated subscripts stand for summation, as:

$$f_L = \alpha_1(P_1^2 + P_2^2 + P_3^2) + \alpha_{11}(P_1^4 + P_2^4 + P_3^4) + \alpha_{12}(P_1^2P_2^2 + P_1^2P_3^2 + P_2^2P_3^2)$$

$$+ \alpha_{111}(P_1^6 + P_2^6 + P_3^6) + \alpha_{112}[P_1^4(P_2^2 + P_3^2) + P_2^4(P_1^2 + P_3^2) + P_3^4(P_1^2 + P_2^2)]$$

$$+ \alpha_{123}\left(P_1^2P_2^2P_3^2\right), \tag{S2}$$

$$f_{elas} = \frac{1}{2}C_{ijkl}e_{ij}e_{kl} = \frac{1}{2}C_{ijkl}\left(\varepsilon_{ij} - \varepsilon_{ij}^0\right)\left(\varepsilon_{kl} - \varepsilon_{kl}^0\right), \tag{S3}$$

$$f_{dip} = -\frac{1}{2}E_i^dP_i, \tag{S4}$$

$$f_{dep} = -\frac{1}{2}E_i^{dep}P_i, \tag{S5}$$

$$\begin{aligned} f_{grad} = {} & \frac{1}{2}G_{11}\left(P_{1,1}^2 + P_{2,2}^2 + P_{3,3}^2\right) + G_{12}\left(P_{1,1}P_{2,2} + P_{2,2}P_{3,3} + P_{3,3}P_{1,1}\right) \\ & + \frac{1}{2}G_{44}\left[\left(P_{1,2} + P_{2,1}\right)^2 + \left(P_{2,3} + P_{3,2}\right)^2 + \left(P_{1,3} + P_{3,1}\right)^2\right] \\ & + \frac{1}{2}\left[\left(P_{1,2} - P_{2,1}\right)^2 + \left(P_{2,3} - P_{3,2}\right)^2 + \left(P_{1,3} - P_{3,1}\right)^2\right] \end{aligned} \tag{S6}$$

where α_1, α_{11}, α_{12}, α_{111}, α_{112}, α_{113} are the dielectric stiffness coefficients; C_{ijkl} is the fourth-rank elastic constant tensor with three independent elastic constants C_{11}, C_{12} and C_{44} in Voigt's notation for cubic materials; e_{ij} is the elastic strain; ε_{ij} is the total strain; ε_{ij}^0 is the stress-free eigenstrain (or the spontaneous strain) denoted by $\varepsilon_{ij}^0 = Q_{ijkl}P_kP_l$, where Q_{ijkl} is the fourth-rank electrostrictive coefficient tensor of the system with three independent electrostrictive coefficients Q_{11}, Q_{12} and Q_{44} in Voigt's notation; $E_i^{dep} = -\bar{P}_i/\kappa_{ii}$ is the depolarization field due to the uncompensated surface charges, and $\bar{P}_i$is the average polarization; G_{11}, G_{12}, G_{44} and G'_{44} are the gradient energy coefficients; $E_i^d$is the dipole-dipole interaction electric field obtained by solving the electrostatic equilibrium condition

$$D_{i,i} = \varepsilon_0\kappa_{ii}E_{j,i}^d + P_{i,i} \tag{S7}$$

where $D_{i,i} = \partial D_i/\partial x_i$, $E^d_{j,i} = \partial E^d_j/\partial x_i$, $P_{i,i} = \partial P_i/\partial x_i$ and $\varepsilon_0 = 8.85 \times 10^{-12} F/m$ is the dielectric permittivity of vacuum, assuming the relative dielectric permittivity $\kappa_{ij}=0$ for $i \neq j$. The solution of Eq. S7 leads to Eq.4 and Eq. 5 in the manuscript.

For epitaxial ferroelectric thin films, boundary conditions were considered as stress-free at the top surface and strain-free at the bottom surface with short-circuit condition. The electrical potential solution was separated as the combination $\phi = \phi^A + \phi^B$, in which ϕ^A was solved the electrostatic equilibrium via Eq. S7, and ϕ^B was solved by the short-circuit condition:

$$\phi|_{h_{int}} = \phi|_{h_f} = 0 \tag{S8}$$

where h_{int} and h_{f} are the positions of bottom and top surfaces, respectively. ϕ^B was then solved by:

$$\phi^B_{,11} + \phi^B_{,22} + \phi^B_{,33} = 0, \tag{S9}$$

where $\phi^B_{,ii} = \partial^2 \phi^B/\partial x_i^2$. Considering the asymmetrical boundary condition (stress-free at the top surface and strain-free at the bottom surface), 2D Fourier transform was applied for Eq. S9, leading to:

$$-\kappa_{11}\eta_1^2\hat{\phi}^B - \kappa_{22}\eta_2^2\hat{\phi}^B + \kappa_{33}\frac{\partial^2}{\partial x_3^2}\hat{\phi}^B = 0 \tag{S10}$$

where η_1 and η_2 are the wave vectors in Fourier space, and $\hat{\phi}^B$ is the Fourier transform of . Subsequently, partial derivative equation and the solution can be formed:

$$\frac{\partial^2}{\partial x_3^2}\hat{\phi}^B = \hat{\phi}^B\frac{\kappa_{11}\eta_1^2 + \kappa_{22}\eta_2^2}{\kappa_{33}} \tag{S11}$$

$$\hat{\phi}^B(\eta_1,\eta_2,x_3) = c_1(\eta_1,\eta_2)exp\left(x_3\sqrt{\frac{\kappa_{11}\eta_1^2 + \kappa_{22}\eta_2^2}{\kappa_{33}}}\right) + c_2(\eta_1,\eta_2)exp\left(-x_3\sqrt{\frac{\kappa_{11}\eta_1^2 + \kappa_{22}\eta_2^2}{\kappa_{33}}}\right). \tag{S12}$$

The coefficients $c_1(\eta_1,\eta_2)$ and $c_2(\eta_1,\eta_2)$ were then obtained. Considering zero electric field at both surfaces, one more partial derivative equation at the origin of 2D Fourier space $\eta_1 = \eta_2 = 0$ was obtained with solution:

$$\left.\frac{\partial^2}{\partial x_3^2}\hat{\phi}^B\right|_{\eta_1 = \eta_2 = 0} = 0 \tag{S13}$$

$$\hat{\phi}^B = Mx_3 + N. \tag{S14}$$

The full solution of electrical potential at the equilibrium state was obtained by solving the partial derivative equations.

To avoid oversize exponent that might cause invalid data during the time evolution, a set of normalization parameters (α_0, P_0, G_0, κ_0, l_0 and t_0, with $l_0 = \sqrt{G_0/\alpha_0}$ and $L = 1/\alpha_0 t_0$) were introduced to substitute all of the physical parameters with the dimensionless counterparts according to:

$$P^* = \frac{P}{P_0}, \quad C^*_{ijkl} = \frac{C_{ijkl}}{\alpha_0 P_0^2}, \quad Q^*_{ijkl} = Q_{ijkl} \cdot P_0^2, \quad E^* = \frac{E}{\alpha_0 P_0},$$
$$G^* = \frac{G}{G_0}, \quad \kappa^*_0 = \kappa_0 \cdot \alpha_0, \quad r^* = \frac{r}{l_0}, \quad t^* = \frac{t}{t_0},$$
$$\alpha^*_1 = \frac{\alpha_1}{\alpha_0}, \quad \alpha^*_{11} = \frac{\alpha_{11} P_0^2}{\alpha_0}, \quad \alpha^*_{12} = \frac{\alpha_{12} P_0^2}{\alpha_0}, \quad \alpha^*_{111} = \frac{\alpha_{111} P_0^4}{\alpha_0},$$
$$\alpha^*_{112} = \frac{\alpha_{112} P_0^4}{\alpha_0}, \quad \alpha^*_{123} = \frac{\alpha_{123} P_0^4}{\alpha_0}. \tag{S15}$$

The values of the parameters for PZT in the phase-field model were used in this work[1]. The grid of size 256×256×64 ($dx^*=dy^*=dz^*=1$) was applied for the polarization evolution, subjected to the time-dependent Landau-Ginzburg equation:

$$\frac{\partial P^*_i}{\partial t^*} =- L\frac{\delta F^*}{\delta P^*_i} \, (i = 1,2,3) \quad . \tag{S16}$$

The second-order backward difference method was applied for the discretization of the time evolution. Equilibrium was indicated by the stabilization of total free energy F, leading to the domain patterns at the equilibrium state as shown in Fig. S1(a). The effects of external electric field were taken into account by adding a free energy density term $- 1/2 \cdot E_i P_i$ to the total free energy, where E_i is the external electric field. As a result, the calculated polarization-electric field hysteresis loops in Fig. S1(b) exhibited typical ferroelectric properties. Therefore, reliable relations between the internal field and polarization was obtained in Fig. S1(c), with linear relations seen in Fig. S1(d).

Supplementary Note 2 . Methods of ACTS for PZT.

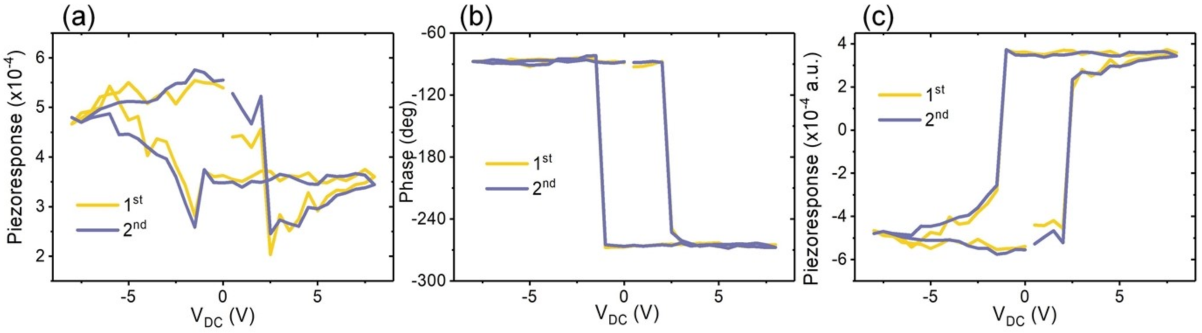

Fig. S2 PFM hysteresis loops for PZT. (a) Amplitude, (b) phase and (c), piezoresponse of the selected as-grown grain of PZT.

All the experiments were conducted at the same position. The PFM hysteresis loops of the grain in question for the PZT in Fig. S2 show clear ferroelectricity. Butterfly-shaped double loops were observed in the amplitudes (Fig. S2(a)). A sharp change in phase with a difference of approximately 180° suggested polarization switching between the two stable polarization states. Typical PFM hysteresis loops, which are characteristic of ferroelectric materials, were subsequently obtained. These results indicated that the selected grains were suitable for studying ACTS.

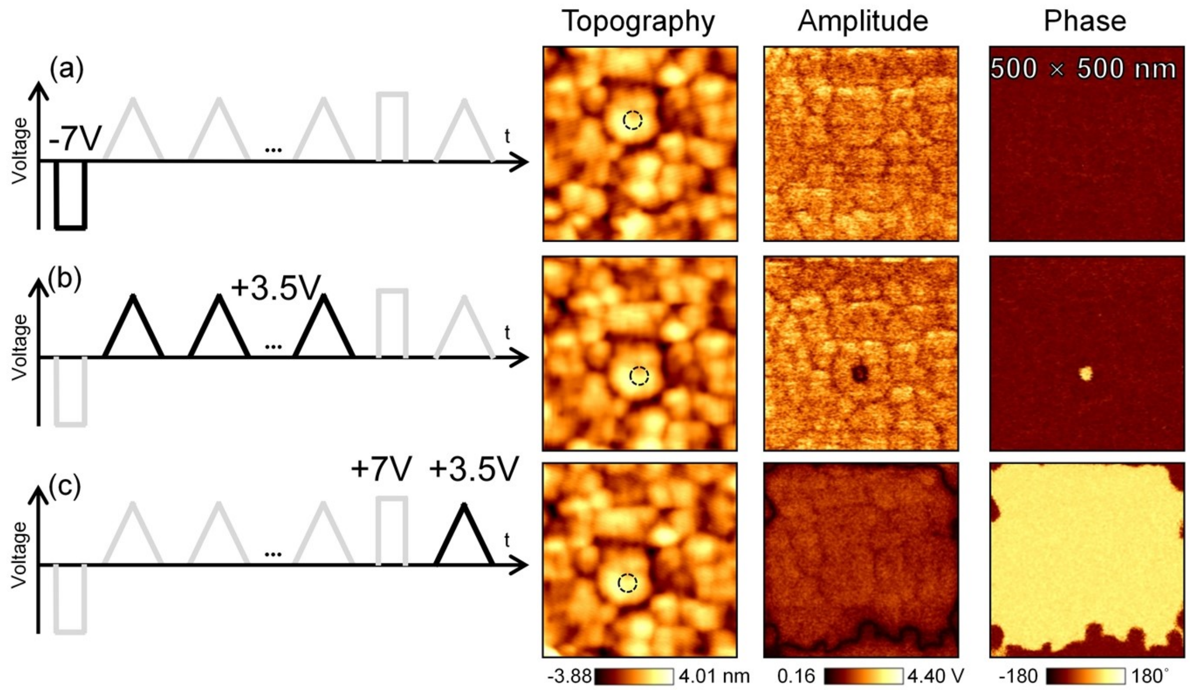

Fig. S3 PFM images for PZT during ACTS. (a). After the background pre-poling. (b). After ACTS waveforms. (c). After the last waveform for determining non-switching current. From left to right are the schematics of ACTS process, topography, PFM amplitude and PFM phase images of PZT, respectively.

Piezoresponse was measured at a single point inside the grains (Fig. S3(a)). The PFM results are shown in Fig. S3(a), which indicates that background poling covered the entire grain and the surrounding grains, ensuring homogeneous prepoled polarization states of the grain in question. Therefore, this grain was deemed suitable for this study. ACTS with various amplitudes and frequencies were conducted at the same point inside the grains. The ACTS waveforms switched a small area in the grain without influencing its neighborhood, as shown in Fig. S3(b). Compared with the AFM-PUND, in which a switched area with a radius of 200 nm was observed, a switching area with a radius as small as 20 nm was managed for ACTS, as shown in Table S1. A stable and large post-poled state area was observed, and the waveform used to detect I_{NS} did not influence the post-poled state, as shown in Fig. S3(c).

Table S1. Comparison of sensitivity between AFM-PUND and ACTS.

	AFM-PUND	ACTS
Amplitude (MV/m)	133	6.66
Switched area radius (nm)	200	20

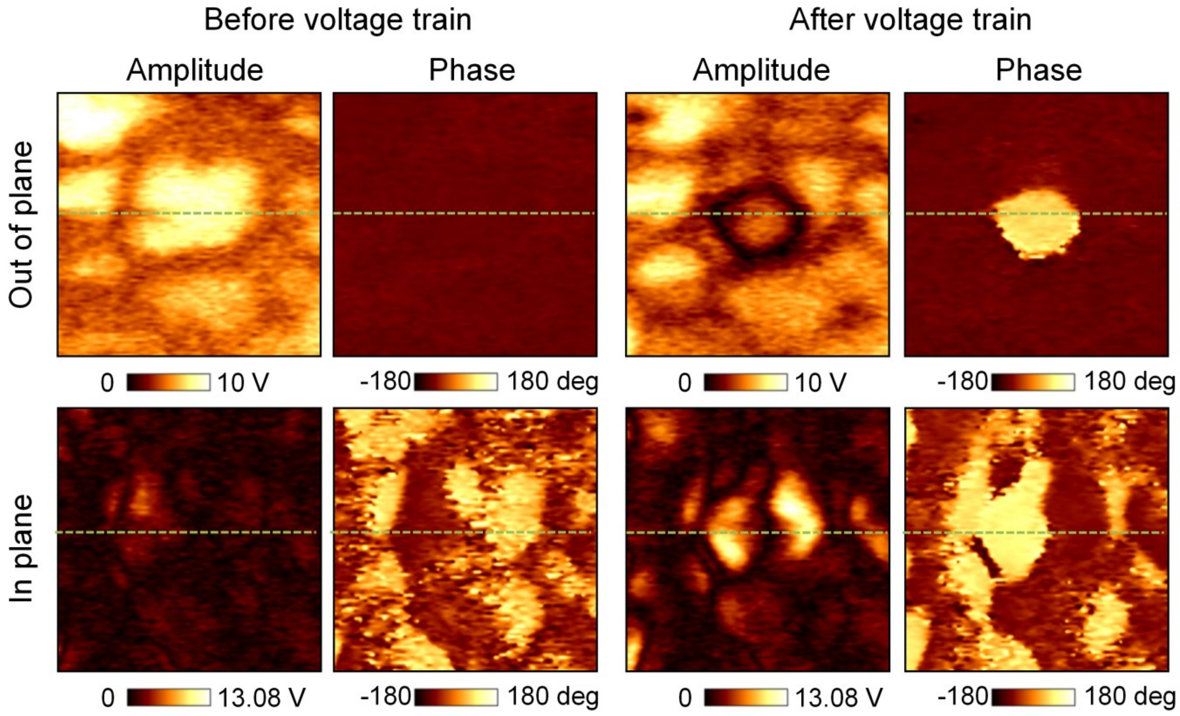

Fig. S4 Out-of-plane and in-plane PFM amplitude and phase images before and after the voltage train in ACTS.

As discussed in the manuscript, phase-field simulations unveils possible 90-degree switching by ACTS. Conventional PFM reveals only the information related to polarization dipoles perpendicular to the sample surface, lacking the information of the parallel case, which is relevant to 90-degree switching. Therefore, the in-plane PFM was conducted simultaneously with the out-of-plane PFM to study 90-degree switching as shown in Fig. S4. Existence of 180-degree switching was verified by the clear phase contrast of the out-of-plane phase image. Decrease of out-of-plane amplitude was also observed at the edge of the switched area, suggesting possibility of 90-degree switching or domain walls. Clear change of in-plane phase indicates change of in-plane polarization by the voltage train. At the edge of the switched area indicated by the out-of-plane amplitude is the increase of in-plane amplitude, revealing 90-degree switching. Corresponding line data along the dashed line were exhibited in Fig. 2f in the manuscript.

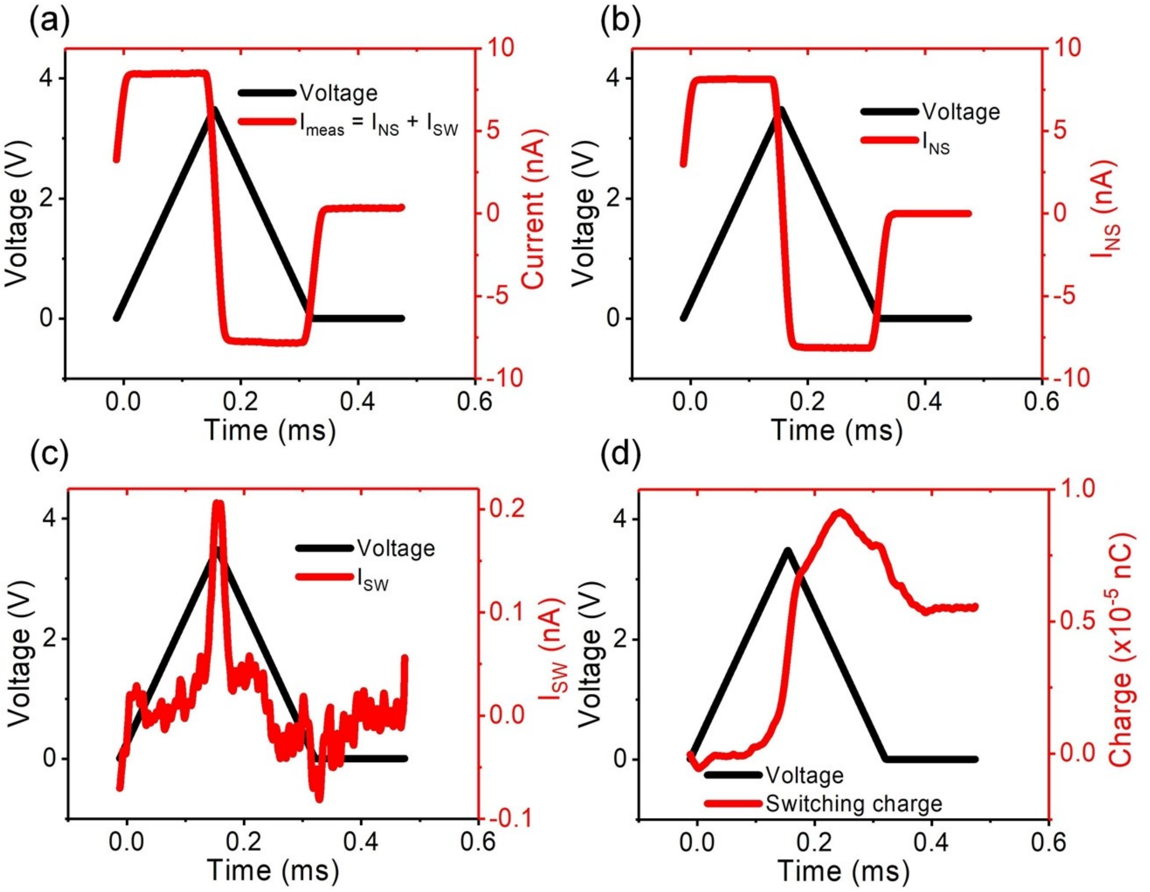

Fig. S5 ACTS results at the first waveform for PZT. (a). Measured current $I_{\mathrm{meas}} = I_{\mathrm{NS}} + I_{\mathrm{SW}}$. (b). Non-switching current I_{NS}. (c). Switching current I_{SW}. (d). Switching charge of the first waveform with amplitude of 3.5 V at 2 kHz.

The measured currents I_{meas} at the first waveform of the ACTS and I_{NS}, which were measured at the last waveform, exhibited no clear differences, as shown in Figs. S5(a, b), because the voltage amplitude was only slightly higher than V_{C}. Therefore, the switching current I_{SW}, which was obtained using I_{meas} - I_{NS}, showed a typical ferroelectric switching current peak (Fig. S5(c)). The integral of I_{SW} with respect to time, by which the switching charge was obtained, also exhibited typical ferroelectric behavior (Fig. S5(d)).

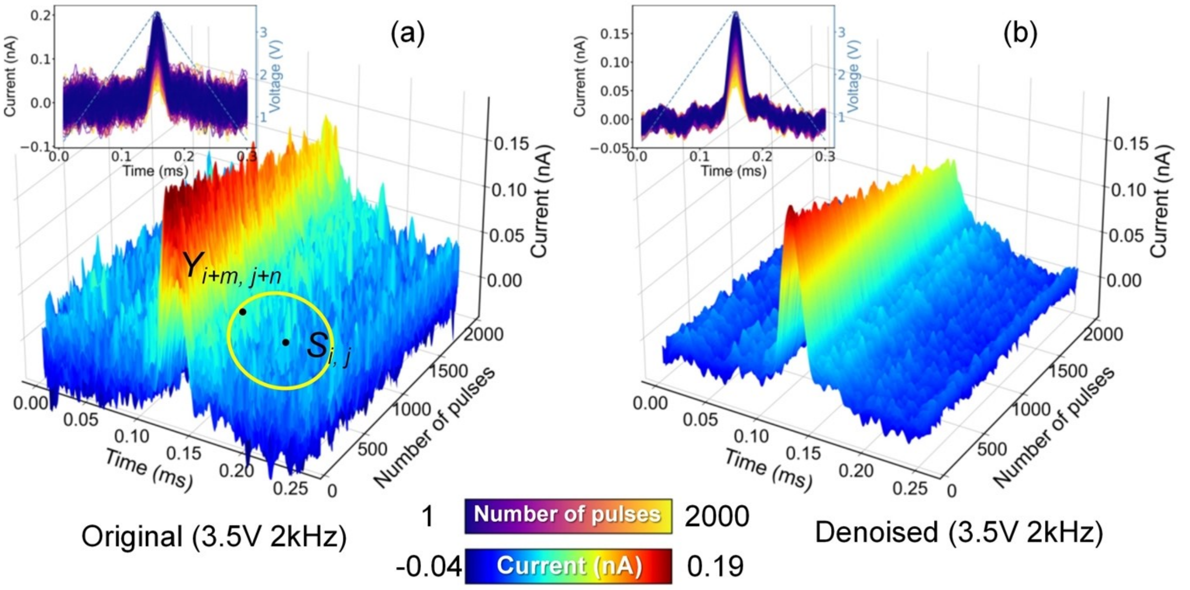

Fig. S6 Denoising results for I_{SW}. Switching current for PZT at 3.5 V and 2 kHz as a function of time and number of waveforms (a) before and (b) after denoising. The inset shows switching current as a function of time at different number of waveforms.

As shown in Fig. S6(a), the obtained I_{SW} at each waveform showed clear switching peaks, and the peak values decreased with the number of waveforms, implying ferroelectric behavior, as discussed in the manuscript. However, noisy data require further manipulation to reduce the noise level. We extended the previous denoising method[2] to a 2D case using a moving kernel method, in which a single denoised data point $S_{i,j}$ was determined by

$$S_{i,j} = \sum_{m,n}^{N} W\left(D_{i+m,j+n}\right) Y_{i+m,j+n} \Big/ \sum_{m,n}^{N} W\left(D_{i+m,j+n}\right) \tag{S17}$$

where i and j iterate all data points $Y_{i,j}$ in the kernel and W is the weight function expressed as

$$W\left(D_{i+m,j+n}\right) = 1 - D_{i+m,j+n}^{2} \tag{S18}$$

where $D_{i+m,j+n}$ is the normalized distance between $S_{i,j}$ and $Y_{i+m,j+n}$ is the radius of the kernel. To avoid mutual influence between different waveforms, an oval-shaped kernel was selected with a radius along the time axis of 7 and a radius along the number of waveform axes of 5. The good denoising results are shown in Fig. S6(b) with the characterizations maintained.

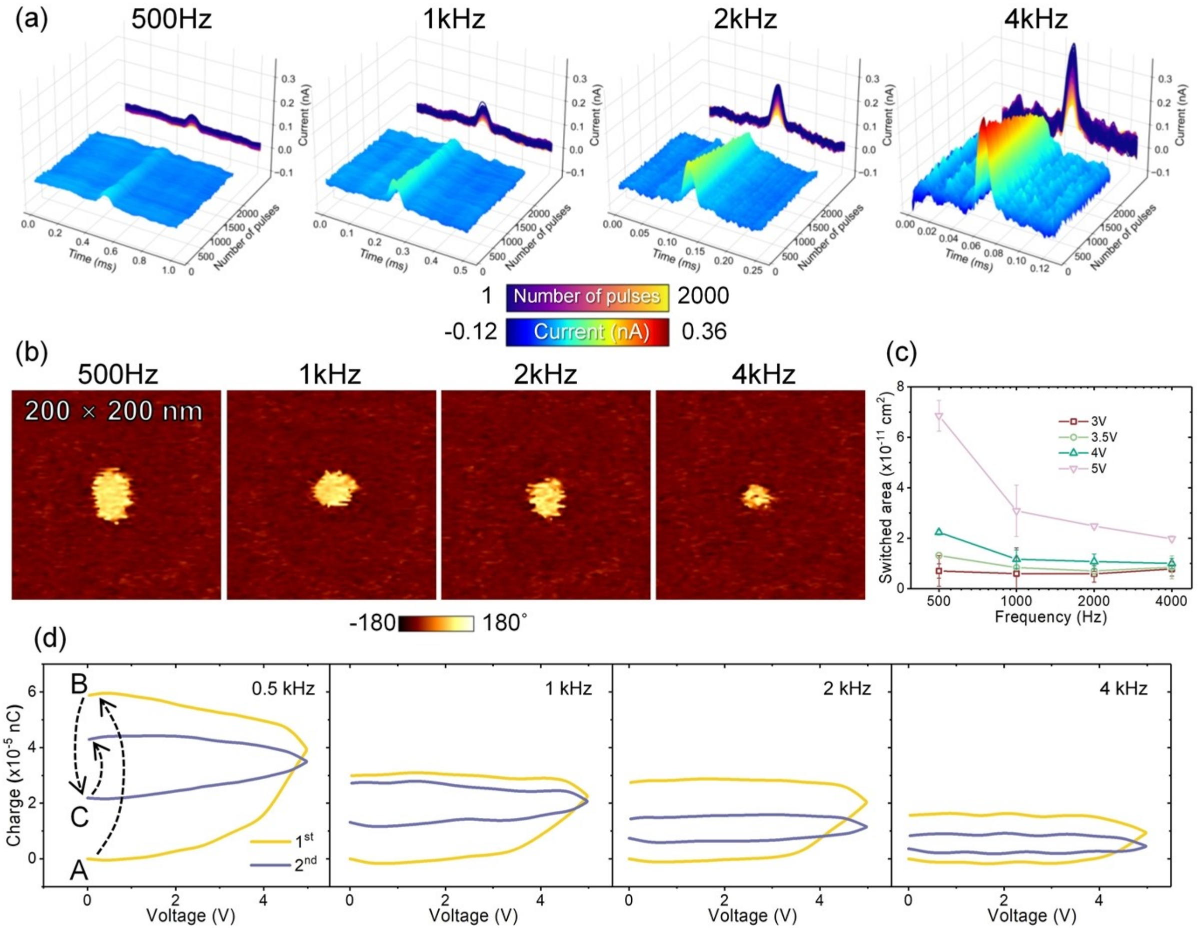

Fig. S7 Denoised ISW and switched area for the amplitude of 3.5V at various frequencies. (a). Switching current of PZT with amplitude of 3.5V as a function of time and number of waveforms with the projection with respect to the number of waveforms showing in the current-time plane for 500, 1k 2k and 4kHz, respectively. (b). PFM phase images after ACTS waveforms with amplitude of 3.5V at 500, 1k, 2k and 4kHz, respectively. (c). Switched area at various ACTS amplitudes and frequencies calculated from the PFM phase images. (d). Charge-voltage hysteresis loops of the first two waveforms for the ACTS amplitude of 5V at various frequencies.

The influence of different frequencies on I_{SW} was similar to previous results that higher frequencies led to lower I_{SW}[4]. In addition, higher frequencies and lower amplitudes resulted in smaller switched areas, as shown in Figs. S7(b, c), leading to a lower switching charge. However, simply comparing I_{SW} at different frequencies was not sufficient because different switching areas were obtained at different frequencies, as shown in Fig. S7(d). Clear hysteretic behaviors were observed for all frequencies, with the loops becoming more unsaturated as the frequency increased to 4 kHz. Overall, the switching decreased as the frequency increased. By calculating the switched polarization (the last $C_{\mathrm{SW,\ acc}}$ divided by the switching area), linear behaviors between the frequency and switched polarization in the logarithmic scale could be observed, in accordance with a previous report[3]. Furthermore, a clear switching and back-switching process was observed, as indicated by the dashed arrows in the first panel from the left in Fig. S7(d). From A to B, the first waveform switched between large portions of the polarization under the tip. Withdrawing the voltage, back-switching could be seen from B to C, suggesting that large portions of the polarizations switched by the tip-induced electric field were partially switched and could be easily back-switched.

Supplementary Note 3. ACTS for TiO_2.

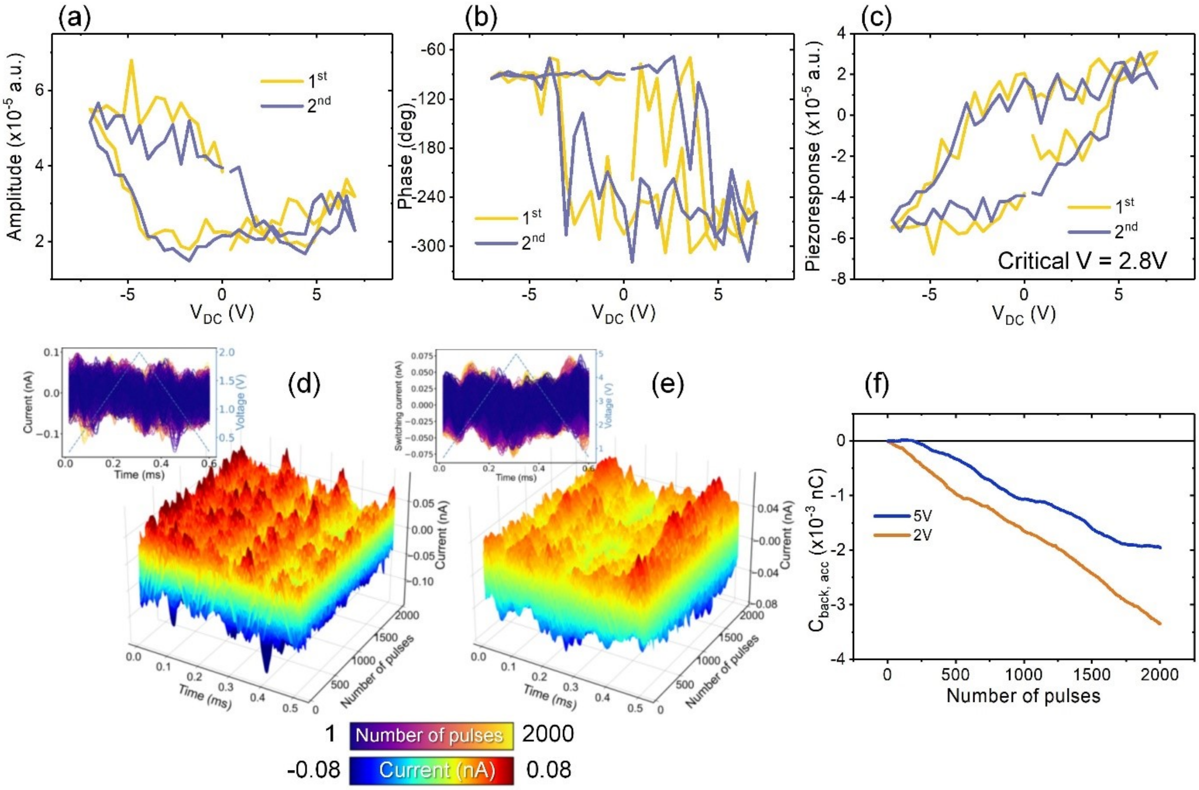

Fig. S8 ESM and denoised ACTS results for TiO_2. (a). Amplitude, (b) phase and (c) ESM response of the selected as-grown grain of TiO_2. (d, e) Switching current at (d) 2 V and (e) 5 V at 1 kHz as a function of time and number of waveforms. The inset shows switching current as a function of time at different number of waveforms. (f). $C_{\text{back, acc}}$ as a function of number of waveforms for 2 V and 5 V at 1 kHz.

For TiO_2, PFM hysteresis loops (Figs. S8(a-c)) showed ferroelectric-like properties and could be mistaken for ferroelectricity. For the calculated I_{SW} from the I_{meas} measured during ACTS, no peaks were observed as shown in Figs. S8(d, e). Instead, valleys of I_{SW} were observed at an amplitude of 5 V owing to the accumulative migration of oxygen vacancies, as discussed in the manuscript. A decrease in $C_{\text{back, acc}}$ was observed for both amplitudes (Fig. S7(f)) because of the relaxation of the oxygen vacancies between the waveforms.

Supplementary Note 4 . ACTS for HZO.

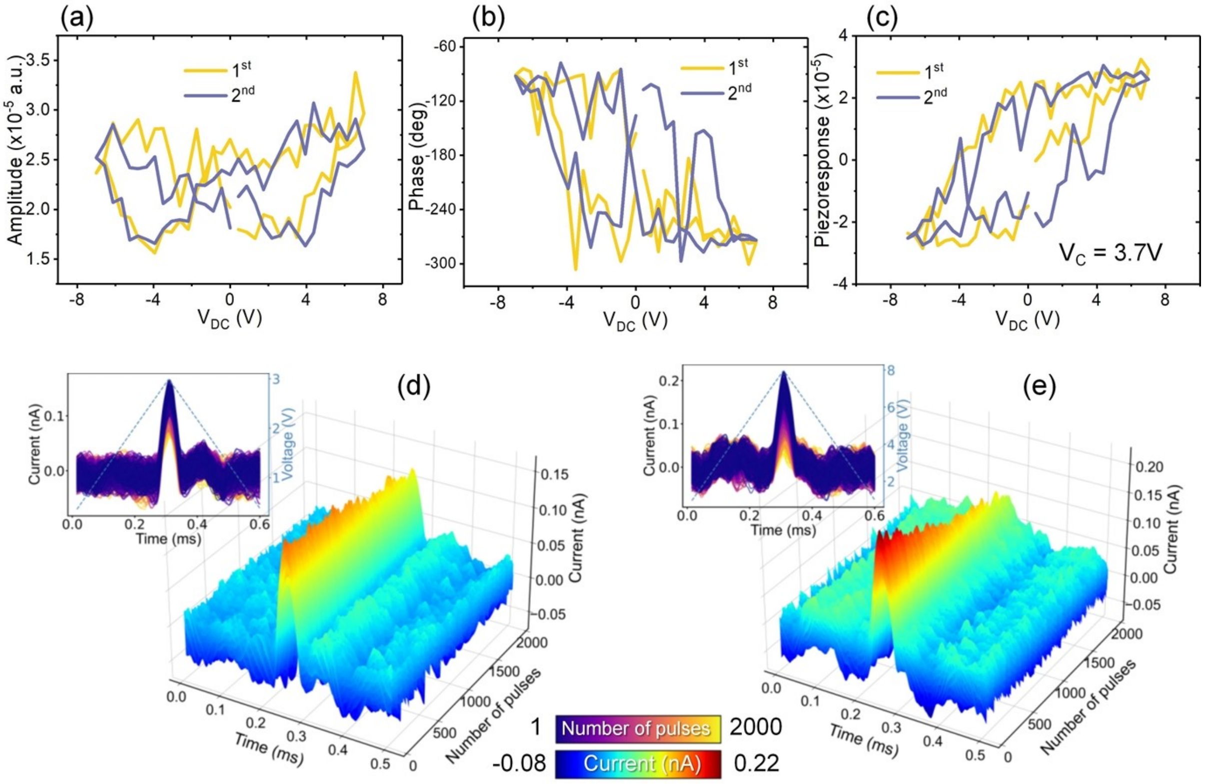

Fig. S9 PFM and denoised ACTS results for HZO. (a) Amplitude, (b) phase and **c** PFM response of the selected as-grown grain of HZO. (d, e) Switching current at (d) 3 V and (e) 8 V at 1 kHz as a function of time and number of waveforms. The inset shows switching current as a function of time at different number of waveforms.

Hysteresis behaviors of the amplitude, phase, and piezoresponse of HZO were also observed, as shown in Figs. S9(a-c), which, as previously discussed, were insufficient for the discrimination of ferroelectricity. The clear I_{SW} peaks are shown in Figure S8. In addition, a decrease in I_{SW} peaks can be seen in Fig. S9, strongly suggesting ferroelectricity owing to the saturation of polarization switching, as discussed in the manuscript. A weak change in the phase images was observed, indicating strong back switching, as discussed in the manuscript.

Supplementary Note 5 . ACTS for FAPbI$_3$.

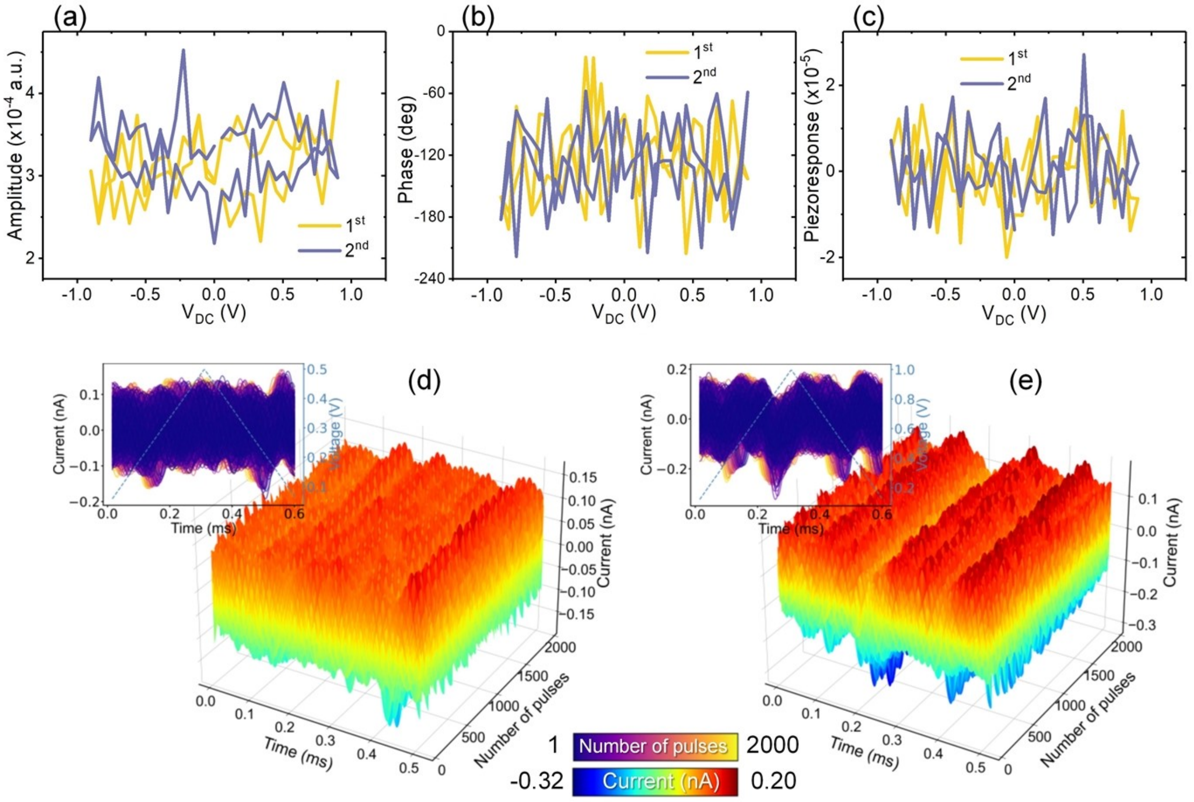

Fig. S10 PFM and denoised ACTS results for FAPbI$_3$. (a) Amplitude, (b) phase and (c) PFM response of the selected as-grown grain of FAPbI$_3$. (d, e) Switching current at (d) 0.5 V and (e) 1 V at 1 kHz as a function of time and number of waveforms. The inset shows switching current as a function of time at different number of waveforms.

In the case of FAPbI$_3$, no clear hysteresis behavior was observed, as shown in Figs. S10(a-c), suggesting nonferroelectric properties. Two and four valleys were observed in I_{SW} for the amplitudes of 0.5 and 1 V respectively (Figs. S10(d, e)) because of the emergence of trap-filled limited (TFL) and trap-free space charge-limited current (SCLC) regions, as discussed in the manuscript.

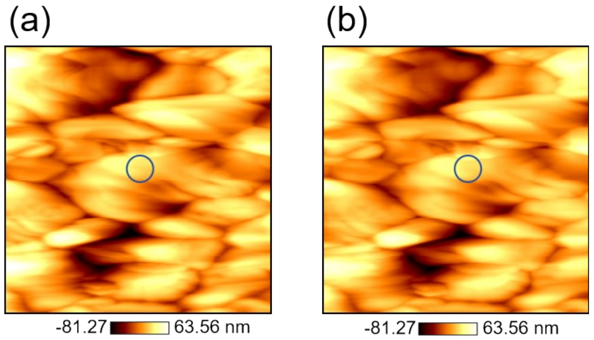

Fig. S11 Topography of $FAPbI_3$ with a size of 2 μm × 2 μm (a) before and (b) after ACTS. The circle indicates the tip position for ACTS.

The topography images of $FAPbI_3$ before and after ACTS were measured by AFM. No observable topography change was observed, suggesting that the application of ACTS did not induce notable redox reactions. Nevertheless, redox cannot be fully excluded due to the shifts of valleys in Figs. 4(d, e) as discussed in the manuscript.

References

1. Wang, J.; Shi, S.-Q.; Chen, L.-Q.; Li, Y.; Zhang, T.-Y., Phase-field simulations of ferroelectric/ferroelastic polarization switching. *Acta Mater.* **2004,** *52* (3), 749-764.

2. Kwon, O.; Kang, S.; Jo, S.; Kim, Y. D.; Han, H.; Park, Y.; Lu, X.; Lee, W.; Heo, J.; Alexe, M.; Kim, Y., Quantitative Local Probing of Polarization with Application on HfO_2-Based Thin Films. *Small Methods* **2021,** *5* (11), 2100781.

3. Scott, J. F., Models for the frequency dependence of coercive field and the size dependence of remanent polarization in ferroelectric thin films. *Integrated Ferroelectrics* **1996,** *12* (2-4), 71-81.

4. Kwon, O.; Seol, D.; Lee, D.; Han, H.; Lindfors-Vrejoiu, I.; Lee, W.; Jesse, S.; Lee, H. N.; Kalinin, S. V.; Alexe, M.; Kim, Y., Direct Probing of Polarization Charge at Nanoscale Level. *Adv. Mater.* **2018,**

30 (1), 1703675.